

1 Solute effects on dynamics and deformation of  
2 emulsion droplets during freezing

3 Sidhanth Tyagi<sup>1,2</sup>, Cécile Monteux<sup>2,3</sup>, and Sylvain Deville<sup>4</sup>

4 <sup>1</sup>*Laboratoire de Synthèse et Fonctionnalisation des Céramiques, UMR 3080*  
5 *CNRS/Saint-Gobain CREE, Saint-Gobain Research Provence, Cavaillon, France.*

6 <sup>2</sup>*Sciences et Ingénierie de la Matière Molle, ESPCI Paris, PSL Research University,*  
7 *CNRS, Sorbonne Universités, UPMC Univ Paris 06, Paris, France.*

8 <sup>3</sup>*Global Station for Soft Matter, Global Institution for Collaborative Research and*  
9 *Education, Hokkaido University, Sapporo, Japan.*

10 <sup>4</sup>*Université de Lyon, Université Claude Bernard Lyon 1, CNRS, Institut Lumière*  
11 *Matière, 69622 Villeurbanne, France.*

12 February 15, 2022

13 **Abstract**

14 Soft or rigid particles, suspended in a liquid melt, interact with an advancing  
15 solidification front in various industrial and natural processes, such as fabrica-  
16 tion of particle-reinforced-composites, growth of crystals, cryopreservation, frost  
17 heave, and growth of sea ice. The particle dynamics relative to the front de-  
18 termine the microstructure as well as the functional properties of the solidified  
19 material. The previous studies have extensively investigated the interaction of  
20 foreign objects with a moving solid-liquid interface in pure melts while in most  
21 real-life systems, solutes or surface active impurities are almost always present.  
22 Here we study experimentally the interaction of spherical oil droplets with a

23 moving planar ice-water interface, while systematically increasing the surfac-  
24 tant concentration in the bulk liquid, using *in situ* cryo-confocal microscopy.  
25 We demonstrate that a small amount of surfactant in the bulk liquid can insti-  
26 gate long-range droplet repulsion, extending over a length scale of 40 to 100  $\mu m$ ,  
27 in contrast to the short-range predicted previously ( $< 1 \mu m$ ). We report on the  
28 droplet deformation, while they are in contact with the ice-water interface, as a  
29 function of the bulk surfactant concentration, the droplet size, and the crystal  
30 growth rate. We also depict the dynamic evolution of solute-enriched premelted  
31 films ( $\approx 5 \mu m$ ). Our results demonstrate how an increasing concentration of  
32 surfactant in the bulk and its subsequent segregation during solidification can  
33 dramatically alter the solidification microstructures. We anticipate that our  
34 experimental study can serve for the development of theoretical models incor-  
35 porating solute effects.

36 *Keywords: solidification, solute, droplets, deformation, dynamics*

# 37 1 Introduction

38 The interaction of particles with an approaching solid-liquid interface is of spe-  
39 cial relevance in nature, like frost heave, glacial motion [1], and in engineering  
40 sciences, such as food freeze-thaw stability [2], cryopreservation [3, 4], metal-  
41 lurgy [5], and crystal growth [6]. This dynamic problem consists of particles,  
42 soft or hard, dispersed in a liquid melt interacting with a solid-liquid interface.  
43 The objects can be biological cells in cryopreservation [3, 4], colloids in freeze-  
44 casting [7], droplets in food preservation [8], gas bubbles in growth of single  
45 crystals [6, 9] and metallurgy [5], or reinforcing particles in material-matrix-  
46 composites [10]. The outcome of the particle-interface confrontation determines  
47 the solidified microstructure and hence, the functional properties of the solidified  
48 material.

49 It is essential to understand the underlying mechanisms of solidification (or  
50 freezing) to forge the required material microstructure. The particle can inter-  
51 act with an advancing solidification interface with diverse outcomes; it can be  
52 engulfed instantaneously upon contact, pushed ahead in the remaining liquid by  
53 the interface indefinitely, or it may undergo engulfment after being pushed over  
54 a certain distance [11]. The shape of the particle (deformed or undeformed)  
55 becomes an equally important processing criterion in applications where soft  
56 deformable objects (droplets or bubbles) encounter a moving solid-liquid in-  
57 terface. Numerous interaction scenarios, still poorly understood, can therefore  
58 exist during solidification.

59 The role and concentration of solute in the solidifying liquid is often signifi-  
60 cant and a dominating factor in determining, amongst others, the shape of the  
61 solid-liquid interface in the vicinity of the suspended particles [12–14]. Solutes  
62 render the interfacial curvature concave, thereby promoting engulfment of ob-  
63 jects at growth rates lower than those predicted for planar curvatures [15, 16].  
64 The solutes can be either desired, like additives (e.g. cryoprotectant used in  
65 preservation of biological cells), or be present as an undesired impurity, such as

66 dissolved gases ( $H_2$ ) in liquid metals or surface active impurities. The segregation  
67 tion of solutes at the interface is instigated by their relatively low solubility in  
68 the solid phase and enhanced further by the approaching objects obstructing  
69 their diffusion field [12]. This local solute enrichment is of particular impor-  
70 tance in understanding the nucleation and growth of macroporosity in solid-  
71 ifying melts [13], studying the constitutional supercooling with formation of  
72 premelted films [17, 18], and in determining the osmotic stresses acting on a  
73 freezing biological cell [4, 19] to give a few examples. Moreover, the morphology  
74 of a solid-liquid interface (planar, columnar, or dendritic), determined by the  
75 magnitude of solute concentration gradient build-up ahead of the growing solid,  
76 plays a major role on the final microstructure [12, 20].

77 Past studies have formulated a plethora of analytical and numerical models  
78 expressing the outcome (engulfment or rejection) of objects interacting at close  
79 distances ( $< 10 \text{ nm}$ ) with the solid-liquid interface [15, 21–24]. The models vary  
80 in the mathematical formulation of the features taken into account (e.g. the  
81 inclusion of object-melt thermal conductivity mismatch, solute effects etc...),  
82 while using a similar approach (balance of repulsive and attractive forces be-  
83 tween the object and front) to describe the interaction [11].

84 The study of particle deformation has been of particular interest in the  
85 prediction of pore shape evolution during directional solidification of crystals  
86 to avoid or control porosity defects. Much of the progress in this domain  
87 has been achieved through numerical simulations and post-solidification analy-  
88 sis [25, 26]. *In situ* experimental evidence of solidification dynamics (repulsion  
89 or engulfment) and shape modification have been facilitated using transpar-  
90 ent analogs (e.g. succinonitrile-acetone) with optical microscopes at ambient  
91 temperatures [20, 27] and X-ray transmission microscope at elevated tempera-  
92 tures [13, 28]. However, the volume investigated along with the temporal reso-  
93 lution is limited, while the local solute segregation cannot be visualized. Hence,  
94 the tracking of microstructures where objects interact with a solid-liquid inter-  
95 face in the presence of solute effects remains challenging.

96 In this study, we analyse the interaction of spherical oil droplets with an  
97 advancing ice-water interface using *in situ* cryo-confocal microscopy. We inves-  
98 tigate the impact of an increasing surfactant concentration on the mechanisms  
99 involved at three different stages: droplets in water (water) far from the solidifi-  
100 cation front, droplets in contact with an approaching solid-liquid interface, and  
101 droplets captured in the growing ice. The three interaction stages are crucial  
102 in determining the droplet spatial distribution and shape evolution, and hence,  
103 the solidification microstructure.

## 104 **2 Methods**

### 105 **2.1 Materials**

106 We purchased the oil (propyl benzoate), surfactant (Tween 80), oil fluorophore  
107 (Difluoro2-[1-(3,5-dimethyl-2H-pyrrol-2-ylidene-N)ethyl]-3,5-dimethyl-1H-pyrro-  
108 lato-Nboron), and aqueous fluorophore (Sulforhodamine B) from Sigma-Aldrich.  
109 The fluorophores are referred to as BODIPY (incorporated in oil) and SRhB  
110 (incorporated in water) in the study. We cycled the deionized water through  
111  $0.45 \mu\text{m}$  Nylon membrane filters (VWR International) to remove traces of im-  
112 purities and ensure purity of the emulsions prepared. We chose propyl benzoate  
113 owing to its low melting temperature ( $T_m = -51.6^\circ \text{C}$ ), low solubility in water  
114 ( $0.035 \text{ g}/100 \text{ g}$ ), and similar density to water ( $\rho_{oil} = 1.023 \text{ g} \cdot \text{cm}^{-3}$ ).

### 115 **2.2 Sample Preparation**

116 We prepared the oil-in-water emulsions using a microfluidic setup, as explained  
117 in our previous study [14]. The monodisperse droplets have radii ( $R_1, R_2$ ) of  
118 either  $7.2 \pm 0.4 \mu\text{m}$  or  $30.9 \pm 1.2 \mu\text{m}$ , as shown in Supporting information. The  
119 oil phase consisted of propyl benzoate with  $10^{-4} \text{ M}$  BODIPY to obtain clear  
120 imaging of dispersed droplets at 1% laser power. For the aqueous phase, we used  
121  $10^{-5} \text{ M}$  SRhB solution, as self-quenching was reported at concentrations above  
122  $2 \times 10^{-4} \text{ M}$  [29]. We added Tween 80 ( $HLB = 15$  [30]), a non-ionic surfactant,

123 to the aqueous phase to stabilise the oil droplets. The surfactant Tween 80 (*cmc*  
124 = 13 – 15  $mg \cdot l^{-1}$  [31]) also acts as a solute and hence colligatively depresses  
125 the freezing point of solutions, when its concentration increases locally [14]. We  
126 prepared three aqueous solutions with 0.01, 0.1, and 1 *wt.%* Tween 80 to study  
127 the impact of solute concentration on the solidification dynamics and behaviour  
128 of oil droplets dispersed in an aqueous phase. The surfactant is added as *wt.%* of  
129 the aqueous solution to have an equal concentration in all the solutions prepared.

130 The concentration of surfactants in the bulk solution at which micelles start  
131 forming is known as the *cmc*. Individual surfactant molecules that are in the  
132 system but are not part of a micelle are called monomers [32]. At 1*wt.%* of  
133 Tween 80 in aqueous solution we are  $\approx 600 \times cmc$ . All experiments are therefore  
134 performed above the *cmc* and increasing the surfactant concentration results in  
135 an increase of the number of micelles in solution while the concentration of  
136 surfactant monomers remains approximatively equal to the *cmc*. The presence  
137 of micelles at the given concentration was confirmed by dynamic light scattering  
138 (DLS) analysis. A typical micelle size of 9 *nm* with a corresponding diffusion  
139 coefficient of 30  $\mu m^2 \cdot s^{-1}$  at 273 *K* was obtained from the DLS analysis. The  
140 prepared emulsions were filled through capillarity and solidified in a rectangular  
141 Hele-Shaw cell (height =100  $\mu m$  and volume =100  $\mu l$ ). We fabricated the Hele-  
142 Shaw cell using two glass slides (Menzel, 24  $\times$  60 *mm*, thickness 0.13–0.16 *mm*),  
143 and sealed it with nail-polish at one end to prevent evaporation and leakage.

### 144 2.3 Imaging & Analysis

145 We used a Leica TCS SP8 confocal laser scanning microscope (Leica Microsys-  
146 temes SAS, Germany) equipped with 488 *nm* (blue), 552 *nm* (green) lasers and  
147 two photodetectors (PMT) for image acquisition. The images were captured  
148 for the emission spectra of BODIPY (oil phase) and SRhB (aqueous phase),  
149 using a non-immersive objective (Leica HCX PL APO CS 20 $\times$ ) with a working  
150 distance of 590  $\mu m$ . Ice does not fluoresce and hence, we can simultaneously  
151 detect three phases (oil droplets, unfrozen aqueous phase, and ice) with two

152 photodetectors. In  $2D$ , we used the microscope at a scanning speed of  $600\text{ Hz}$ ,  
 153 with  $1024 \times 1024\text{ pixels}$  for imaging  $775 \times 775\ \mu\text{m}$ , resulting in  $1.7\text{ s}$  per frame.  
 154 We used Fiji [33] for image thresholding in conjunction with Python [34] for  
 155 image and data analysis.

## 156 2.4 Freezing Stage

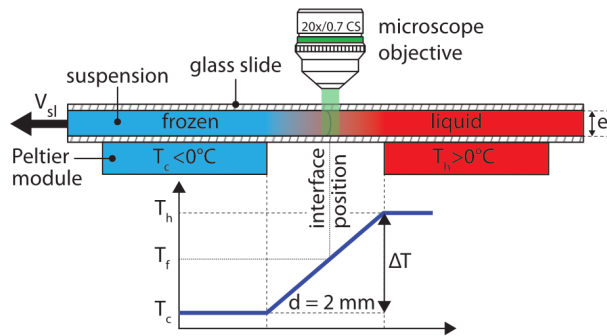


Figure 1: **Cryo-confocal microscope setup to perform *in situ* solidification experiments.** A Hele-Shaw cell containing an oil-in-water emulsion is pulled at a constant velocity ( $V_{sl}$ ) through a constant linear temperature gradient ( $G$ ), established by two Peltier elements. In *steady-state*, the solidification interface is at a constant position under the microscope objective.

157 We conducted unidirectional solidification experiments, translating the sample  
 158 cell at a constant velocity ( $V_{sl}$ ) along a constant linear temperature gradient ( $G$ )  
 159 of  $10^4\text{ K} \cdot \text{m}^{-1}$ , using the cryo-confocal stage described in detail previously [35].  
 160 We imposed the temperature with two Peltier modules, and controlled it with  
 161 high precision ( $< 0.01\text{ }^\circ\text{C}$ ) using TEC-1122 Dual Thermo Electric Cooling Tem-  
 162 perature Controller from Meerstetter Engineering, Switzerland. The Peltier el-  
 163 ements were separated by a distance of  $2\text{ mm}$  to establish a linear temperature  
 164 gradient. The *in situ* observation of objects interacting with the solid-liquid  
 165 interface was achieved using a confocal microscope mounted vertically over the  
 166 gap ( $2\text{ mm}$ ) between the two Peltier modules, as shown in Fig.1. Using this set  
 167 up the solidification interface appears immobile in the frame of observation. We  
 168 utilised the VT-80 translation stage (Micos Pollux Drive PI, USA) to impose  
 169 the rate at the which the sample cell is pulled through the temperature gradi-

ent. The rate of translation was verified to be in agreement with the measured  
solidification velocity ( $V_{sl}$ ), using posterior image analysis ( $error < 1\%$ ). Thus,  
we can decouple and control independently the solidification velocity ( $V_{sl}$ ) and  
the thermal gradient ( $G$ ) in our system.

We performed the solidification experiments in the velocity range of  
 $1.0 \leq V_{sl} \leq 10.0 \mu m \cdot s^{-1}$ . We wait for 20 – 30 mins to ensure a *steady-*  
*state* diffusion controlled regime before starting the acquisition at a given so-  
lidification velocity. The time needed for a steady-state to establish scales as  
 $2D/V_{sl}^2 \approx 60 s$ , where  $D$  is the solute diffusion coefficient. We do not expect  
forced convection in our experiments as they are performed in a closed Hele-  
Shaw cell of small thickness (100  $\mu m$ ) and at low solidification velocity with  
a steady linear temperature gradient. The solid-liquid interface is stable over  
extended time periods ( $\approx 4 - 5 hours$ ) and the interface does not accelerate or  
decelerate during the solidification experiments. In addition, we do not observe  
a transient unsteady regime and the interface morphology is stable for the given  
experimental parameters.

### 3 Results & Discussions

We performed horizontal solidification experiments by displacing a Hele-Shaw  
cell, containing an oil-in-water emulsion, with our custom cryo-confocal stage,  
at a velocity of  $V_{sl}$ . A typical  $2D$  confocal image of a freezing emulsion with  
the distinct features observed is shown in Fig.2A. The confocal image enables  
us to distinguish three phases; oil phase in cyan (fluorophore BODIPY), water  
in colormap viridis (fluorophore SRhB), and a dark ice phase. As solidification  
progresses, the growing ice phase rejects the dissolved dye, SRhB, owing to  
its low solubility and hence appears black, which enables us to visualize the  
solid-liquid interface. In the frame of observation, the interface is stationary.  
In the frame of the sample, the interface is advancing through the sample at a  
velocity of  $V_{sl}$  along  $\vec{x}$  and eventually encounters droplets which velocity, noted



198  $U_r$  (defined in Fig. S2) is indicated in Fig.2A. We also note the premelted films  
199 between two ice surfaces as well as around the oil droplets captured in the ice  
200 phase, which are due to the rejection of the dye by the ice and subsequent  
201 depression of the freezing point.

202 A typical time-lapse evolution of an isolated oil droplet interacting with  
203 the ice-water interface obtained for an oil-in-water emulsion with 1wt.% Tween  
204 80 in the aqueous phase is shown in Fig.2B. The interaction of oil droplets  
205 with the solid-liquid interface can be divided in three different stages, which  
206 are described below in three different sections and which dynamics depends on  
207 the surfactant concentration and advancing velocity. First, we investigate the  
208 solidification mechanisms at play when the oil droplets in the water phase far  
209 from the advancing interface. Secondly we report the evolution of the droplet  
210 shape upon contact with the interface. Third we analyse the droplets captured  
211 in ice and report on the evolution of premelted films with the associated ice-  
212 water meniscus.

### 213 3.1 Droplets in water

214 From each experiment, we acquire 50–400 droplet trajectories and for each tra-  
215 jectory we measure the droplet velocity in the frame of observation  $U' = \delta x / \delta t$   
216 with  $x$  being the distance to the interface and  $t$  the time (see Fig. S1 for the  
217 definition of  $x$  and  $t$ ). We then deduce the velocity of the droplets in the sam-  
218 ple frame  $U_r = V_{sl} - U'$ . We then average over 50 – 400 droplets to obtain  
219 the mean velocity  $\bar{U} = \langle U_r \rangle$  (see details in Fig. S2 and Reference [18] for the  
220 python script). Using these notations, a positive magnitude of  $\bar{U}$  implies that  
221 the droplets are repelled or pushed by the moving ice-water interface towards  
222 the remaining liquid.

223 In Fig.3, we present the mean droplet velocity,  $\bar{U}$ , with the distance to  
224 interface for an interface velocity of  $V_{sl}$  of  $3 \mu m \cdot s^{-1}$ . We define the distance to  
225 interface as  $0 \mu m$  when the front edge of the droplet comes in contact with the  
226 absolute detected position of the ice-water interface.

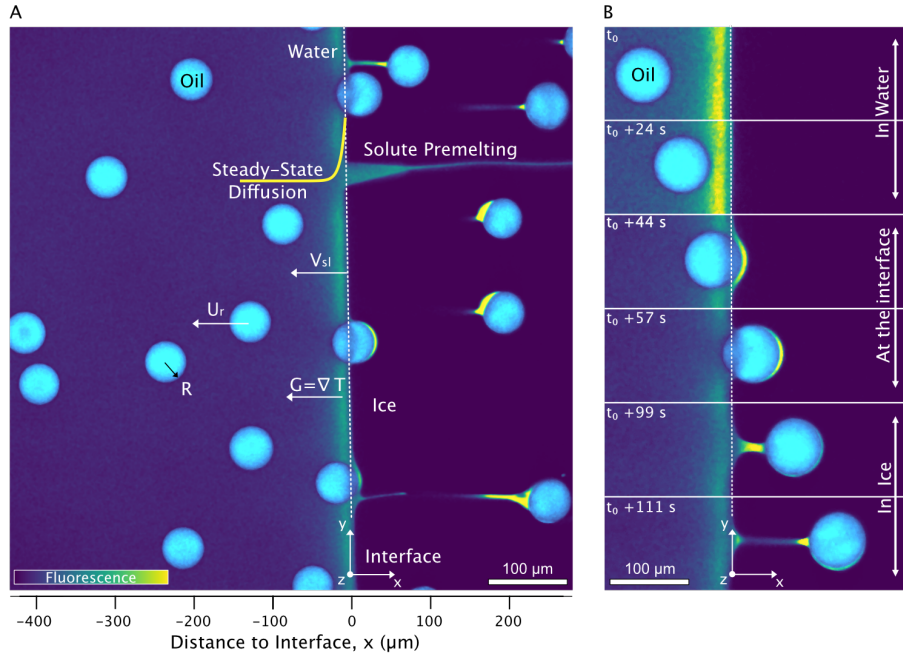


Figure 2: **2D cryo-confocal image of freezing an oil-in-water emulsion in the presence of 1wt.% Tween 80 in the aqueous phase.** (A) Typical features observed for a planar growth at  $V_{sl} = 2 \mu m \cdot s^{-1}$  (B) Time-lapse evolution of an oil droplet encountering an approaching solid-liquid interface with three distinct regimes of interaction at  $V_{sl} = 2 \mu m \cdot s^{-1}$ . Ice is in black, oil droplets in cyan, and the aqueous phase is in colormap viridis (fluorescence bar). © (2020) S. Tyagi *et al.* (10.6084/m9.figshare.14815083) CC BY 4.0 license <https://creativecommons.org/licenses/by/4.0/>.

227 At large distances from the interface, larger than  $100 \mu m$  the droplets in  
 228 water are unperturbed and their mean velocity  $\bar{U}$  in the sample frame is zero.  
 229 As they get closer to the interface, they start getting repelled. The mean droplet  
 230 velocity ( $\bar{U}$ ) increases and exhibits a maximum ( $U_{max}$ ), when the leading edge  
 231 of the droplets coincides with the initial position of the growing crystal. We note  
 232 that the droplet velocity  $\bar{U}$  is lower than  $V_{sl}$ , which means that the droplets are  
 233 finally captured in ice. As the droplets are captured in ice, their velocity  $\bar{U}$   
 234 returns to zero. As shown in Fig.3,  $\bar{U}$  decreases for a larger droplet size, while  
 235 it increases with an increasing surfactant concentration.

236 From the evolution of  $\bar{U}$  with the distance to the interface, we define a char-  
 237 acteristic length scale,  $L_v$ , corresponding to the distance at which the droplets

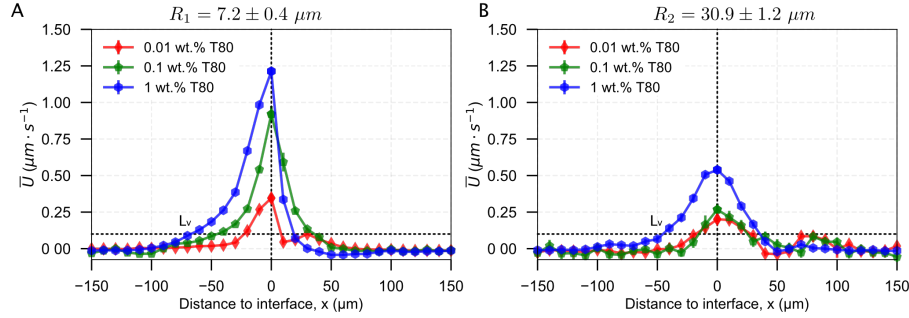


Figure 3: **Droplet dynamics in presence of 0.01, 0.1, and 1wt.% solute in solution, deduced from the droplet trajectories at  $V_{sl} = 3 \mu m \cdot s^{-1}$ .** Mean droplet velocity versus distance to interface for (A)  $R_1 = 7.2 \pm 0.4 \mu m$  and (B)  $R_2 = 30.9 \pm 1.2 \mu m$ . The droplets accelerate as the solidification front approaches, and decelerate as they are engulfed into the ice. © (2020) S. Tyagi *et al.* (10.6084/m9.figshare.14815083) CC BY 4.0 license <https://creativecommons.org/licenses/by/4.0/>.

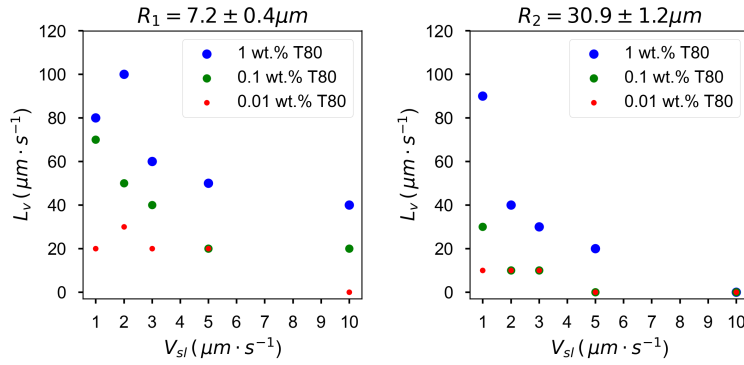


Figure 4: **Characteristic length scale  $L_v$  versus Solidification Velocity ( $V_{sl}$ ), for different solute concentrations (wt.%).** Left:  $R_1 = 7.2 \pm 0.4 \mu m$  and right:  $R_2 = 30.9 \pm 1.2 \mu m$  droplets. The distance  $L_v$ , where droplets in water start getting repelled by the interface, increases significantly with the solute concentration, while it decreases with an increasing growth rate. © (2020) S. Tyagi *et al.* (10.6084/m9.figshare.14815083) CC BY 4.0 license <https://creativecommons.org/licenses/by/4.0/>.

238 attain a mean velocity ( $\bar{U}$ ) of  $0.1 \mu m \cdot s^{-1}$ , which is shown in Fig.4. This distance  
 239 corresponds to the range of interaction between the droplets and the interface.  
 240 We find that the droplets get repelled over distances ranging between 10 and  
 241  $100 \mu m$ , often larger than their diameter, especially for the largest surfactant  
 242 concentrations. Smaller droplets with radius  $R_1$  are repelled at greater distances  
 243 from the interface as compared to the larger  $R_2$  droplets. Increasing the growth

244 rate decreases the characteristic distance  $L_v$ .

245 The results described so far show that an increasing amount of surfactant  
246 induces a repulsion of the droplets by the interface over large distances, of the  
247 order of ten to a hundred of microns away from the interface and that the  
248 droplet dynamics is influenced by the bulk surfactant concentration, the growth  
249 rate and the droplet size. These three parameters control the local gradient of  
250 surfactant concentration close to the solidification front. Indeed the surfactant  
251 concentration close to the solid-liquid interface is higher as compared to the  
252 bulk concentration far from the interface because of its low solubility in ice.  
253 For *steady-state* planar growth, the concentration field of rejected solutes in the  
254 remaining liquid writes

$$C_L = C_0 + C_0 \left( \frac{1 - K_0}{K_0} \right) \exp \left[ \frac{-V_{sl}}{D} |x| \right] \quad (1)$$

255 where  $C_L$  is the solute concentration at a distance  $x$  from the interface,  $C_0$   
256 is the bulk solute concentration in the liquid far from the interface,  $D$  is the  
257 solute diffusion coefficient and  $K_0$ , the partition coefficient defined as the ratio  
258 of surfactant concentration in the solid phase to the one in the liquid [36].

259 In a previous article [18], we suggested that the displacement of the droplets  
260 is caused by surfactant concentration gradients close to the ice-water interface,  
261 possibly through a phenomenon called diffusiophoresis [37]. Diffusiophoresis  
262 is provoked by solute concentration gradients and can lead to displacement of  
263 micrometric particles with velocities of the order of a few micron per second,  
264 comparable to the droplet velocities that we measure in our study. From Eq. (1),  
265 it is expected that the local gradient of surfactant concentration spans over a  
266 typical distance  $L_d = D/V_{sl}$  [36]. Hence an increasing growth rate ( $V_{sl}$ ) will  
267 decrease the distance at which the solute field can be perceived by the droplets  
268 and can qualitatively account for the decreasing values of  $L_v$  measured (see  
269 Fig.4) at high growth rates. Moreover the concentration gradient  $C_L - C_0$   
270 depends linearly on  $C_0$  which can possibly account for the strong influence of

271 the surfactant concentration on the droplet displacement.

272 We note that diffusiophoretic displacements of particles have been studied  
 273 theoretically and experimentally for simple solutes such as ionic salts, dissolved  
 274 gas or charged surfactants such as Sodium dodecylSulfate [37–40] but was never  
 275 reported for non-ionic species.

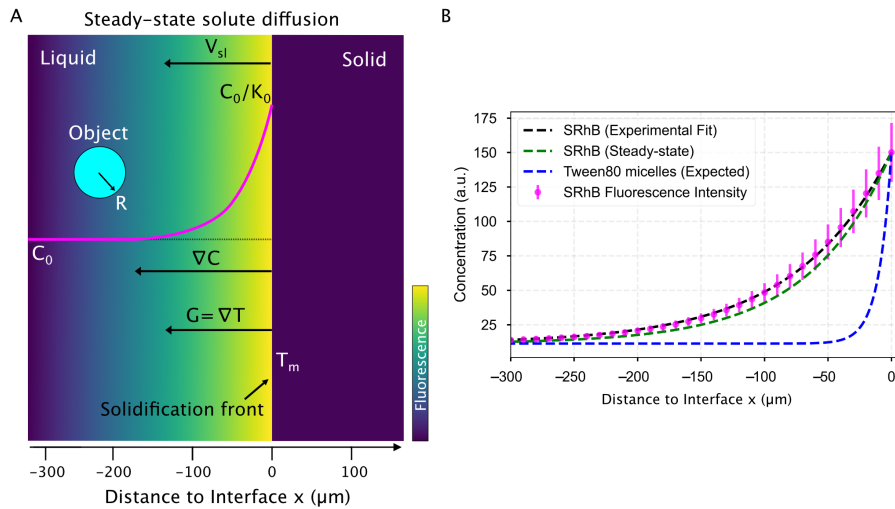


Figure 5: **Solute rejected by the growing solid phase and segregated at the solid-liquid interface during *steady-state* directional solidification.** (A) Model sketch depicting the concentration profile evolution of a solute (in magenta) in the remaining liquid, rejected by a solidification front advancing at  $V_{sl}$ , during *steady-state* planar growth. (B) Mean fluorescence intensity (magenta) of SRhB, acquired using a confocal microscope, is fit with a theoretical diffusion-type exponential (black line). The predicted *steady-state* diffusion of SRhB (green line), using the model from Tiller *et al.* [36], corresponds closely to the experimental data fit. A *steady-state* planar growth is thus verified. The corresponding *steady-state* diffusion profile of Tween 80 micelles (blue) shows a significant difference in length scales over which the two molecules (SRhB and Tween 80) diffuse. All data presented was recorded for a growth rate of  $3 \mu\text{m} \cdot \text{s}^{-1}$ . © (2020) S. Tyagi *et al.* (10.6084/m9.figshare.14815083) CC BY 4.0 license <https://creativecommons.org/licenses/by/4.0/>.

276 To further study the influence of the surfactant concentration gradients on  
 277 the droplet dynamics, it would be useful to measure *in situ* the surfactant  
 278 concentration close to the front. However Tween 80 does not fluoresce, hence  
 279 we cannot measure its concentration profile. However it is in principle possible  
 280 to predict it from Equation 1 provided a steady state regime is reached in our

281 experiments. Therefore we examine the validity of Equation 1 by recording the  
282 fluorescence intensity of the dye, SRhB, which can be obtained easily with the  
283 confocal microscope (see Fig.5A). The concentration profile of SRhB rejected  
284 by the ice-water interface, deduced from the fluorescence intensity profile for a  
285 growth rate of  $3 \mu\text{m} \cdot \text{s}^{-1}$  is given in Fig.5B. At  $3 \mu\text{m} \cdot \text{s}^{-1}$ , the concentration  
286 profile obtained is in agreement with the *steady-state* diffusion profile predicted  
287 from Eq.1 (see Fig.5B). However we note that the *steady-state* approximation  
288 is not valid at higher velocities (not shown) probably because constitutional  
289 undercooling modifies the local temperature of the front hence the diffusion  
290 coefficient of the dye.

291 Interestingly, we see from Fig.5B which is obtained for a velocity of  $3 \mu\text{m} \cdot \text{s}^{-1}$ ,  
292 that the distance at which the dye concentration profile starts increasing is of  
293 the order of  $150 \mu\text{m}$ . This value is much higher than the typical distance  $L_v$   
294 over which both the large and small droplets get repelled from the interface at  
295 the same velocity, which are below  $60 \mu\text{m}$ . As the surfactant monomers and the  
296 dye have the same diffusion coefficient, we would expect that the distance  $L_d$  is  
297 similar for both species.

298 To account for the discrepancy between the measured values of  $L_v$  and the  
299 theoretical  $L_d = D/V_{sl}$ , one may suggest that the droplet dynamics may be con-  
300 trolled by the concentration gradient of surfactant micelles rather than the sur-  
301 factant monomers, which diffusion coefficient is lower than that of the monomers  
302 and for which we expect a lower value of  $L_d$ . Using DLS, we measured the dif-  
303 fusion coefficient of the micelles and calculated the corresponding concentration  
304 profile using Eq.1. As shown in Fig.5B, at a growth rate of  $3 \mu\text{m} \cdot \text{s}^{-1}$ , we obtain  
305 a typical distance  $L_d$  of  $10 \mu\text{m}$ , which is lower than the distance  $L_v$  measured  
306 experimentally at this growth rate. Hence it turns out that the experimentally  
307 measured value of  $L_v$  ranges between the  $L_d$  values calculated either for the  
308 surfactant micelles or for the monomers. However we note that the monomer  
309 and micelle concentration profiles close to ice-water front depends on the ex-  
310 change dynamics between the surfactants and the micelles, hence may not be

311 at equilibrium.

312 The segregation of solute at the interface thus plays a key role in redistribut-  
313 ing the droplets before they hit the solidification front. We believe this can be an  
314 important criterion for controlling the spatial distribution of objects, especially  
315 in multiple object scenarios. The control of the material microstructure has  
316 been a topic of interest in alloy solidification (especially in particle-reinforced-  
317 composites) and for impurity control in castings and single crystal growth. The  
318 object dynamics and impact of solute (or impurity) are still complex to quantify  
319 as the observation of solidification *in situ* remains challenging. We have tried  
320 to advance towards an *in situ* quantification of the solute mechanisms at play  
321 and further work is required to correlate the dye fluorescence intensity to the  
322 absolute solute concentration gradient. The latter can be useful in predicting  
323 thermal convection and non *steady-state* solidification regimes.

### 324 **3.2 Droplets at the interface**

325 We now focus on the behaviour of droplets when they come in contact (distance  
326 to interface =  $0 \mu m$ ) with the solid-liquid interface. We observe three typical  
327 behaviours of oil droplets as they encounter an approaching front, as shown  
328 in Fig.6. The droplets can elongate permanently as they get engulfed in the  
329 growing ice (Fig.6A), the droplets may deform transiently ( $t = 13 s$ ) at the  
330 ice-water interface and subsequently relax to their original spherical shape as  
331 they move further into the ice phase (Fig.6B), or the droplets remain mostly  
332 spherical during their engulfment by the growing crystal (Fig.6C). We notice  
333 that the deformation behaviour depends on the droplet size  $R$ , the imposed  
334 growth rate  $V_{sl}$ , and the bulk surfactant concentration. Therefore, we need to  
335 systematically study the effect of these solidification parameters to understand  
336 the different types of deformation observed.

337 The droplet deformation is estimated from the analysis of  $2D$  shape elonga-  
338 tion, as shown in the schematic in Fig.6A, taking the ratio of droplet diameters  
339 along  $\vec{x}$  and  $\vec{y}$ . In Fig.7, we depict the mean elongation profiles calculated for 50

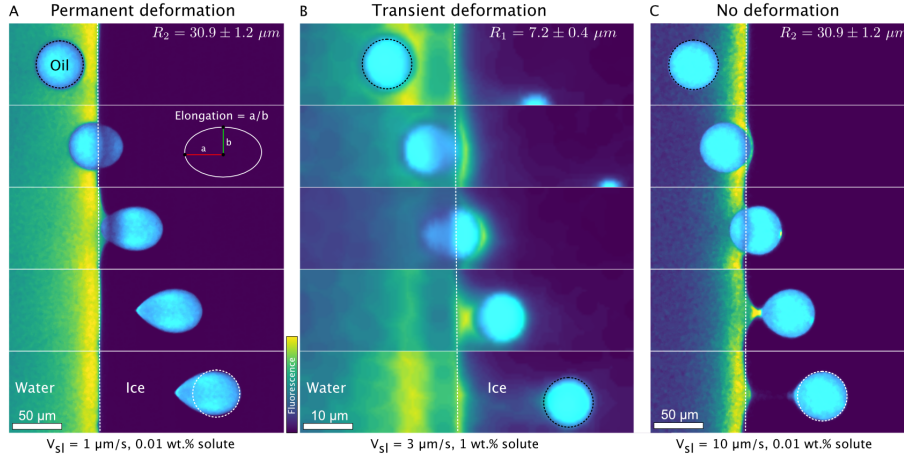


Figure 6: **Typical time-lapse montage depicting the three types of deformation behaviour of oil droplets while undergoing directional planar front solidification.** (A) The droplets elongate at the ice-water interface and remain deformed in the ice phase, scale bar =  $50 \mu\text{m}$ , time interval between frames:  $44.5\text{s}$  (B) The droplets deform in a transient manner ( $t = 13 \text{ s}$ ) at the ice-water interface and recover their shape as they are captured by the growing ice phase, scale bar =  $10 \mu\text{m}$ , time interval between frames:  $6.7\text{s}$  (C) The droplets do not undergo deformation and preserve their shape during their interaction and further engulfment in the growing crystal. Scale bar =  $50 \mu\text{m}$ , time interval between frames:  $3.3\text{s}$ . Oil is in cyan, water is in colormap viridis (fluorescence bar), and ice is in black. © (2020) S. Tyagi *et al.* (10.6084/m9.figshare.14815083) CC BY 4.0 license <https://creativecommons.org/licenses/by/4.0/>.

340 to 400 (depending on  $R$  and  $V_{sl}$ ) droplet interactions in  $0.01 \text{ wt.}\%$  and  $1 \text{ wt.}\%$   
 341 solute solution at varying growth rates for two different droplet sizes ( $R_1, R_2$ ).

342 We observe from Fig.7A and Fig.7B that the droplets undergo permanent  
 343 elongation for the two droplet sizes ( $R_1, R_2$ ), when the bulk surfactant concen-  
 344 tration is  $0.01 \text{ wt.}\%$ . The elongation is  $\approx 1.0$ , representing a circle, when the  
 345 droplets are in the remaining liquid far from the interface. The droplets start  
 346 getting elongated as their front edge touches the interface (distance =  $0 \mu\text{m}$ )  
 347 and their shape transforms into an ellipse (elongation  $> 1.0$ ). The droplet de-  
 348 formation evolves further and reaches a constant magnitude when the front edge  
 349 is located at a distance of  $2R \times \text{Elongation}$ . Once the droplets are completely  
 350 engulfed in the ice, their shape does not evolve any more (Fig.7A,B). Interest-  
 351 ingly, we notice that the elongation reduces with an increasing growth rate for



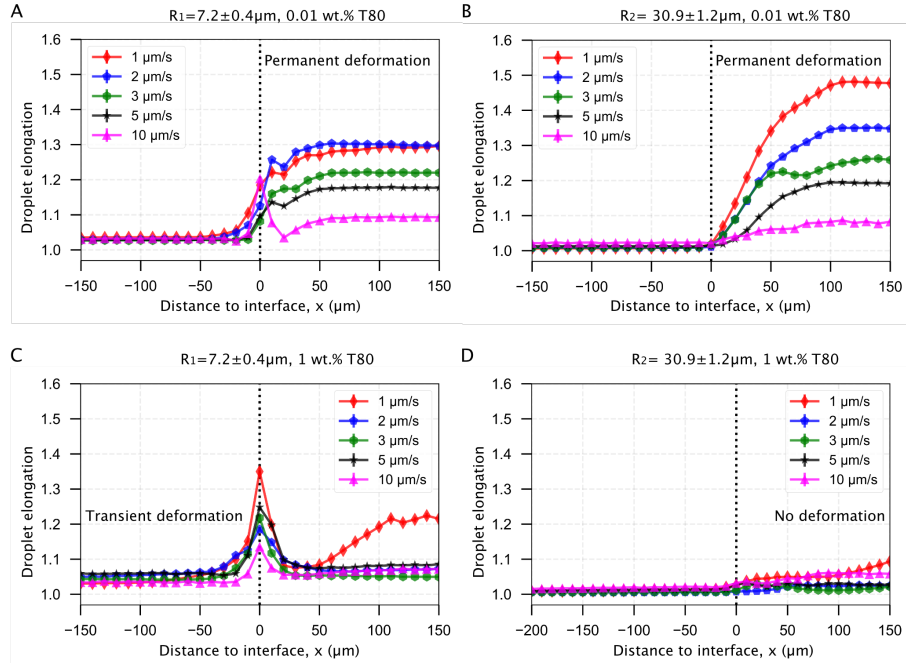


Figure 7: **Mean elongation profiles for oil droplets encountering an approaching ice-water interface.** Planar solidification front induced permanent deformation of oil droplets dispersed in a solution with (A,B) 0.01 *wt.%* solute concentration having a size of (A)  $R_1 = 7.2 \pm 0.4 \mu m$  (B)  $R_2 = 30.9 \pm 1.2 \mu m$ . The transient and no deformation regimes for droplets in (C,D) 1 *wt.%* solute concentration having a size of (C)  $R_1 = 7.2 \pm 0.4 \mu m$  (D)  $R_2 = 30.9 \pm 1.2 \mu m$ . © (2020) S. Tyagi *et al.* (10.6084/m9.figshare.14815083) CC BY 4.0 license <https://creativecommons.org/licenses/by/4.0/>.

352 both the droplet sizes investigated. However, the maximum elongation for the  
 353 smaller  $R_1$  droplets is lower as compared to the larger  $R_2$  droplets at the given  
 354 0.01 *wt.%* solute concentration.

355 In Fig.7C, we report the transient deformation of the oil droplets as they  
 356 confront the ice-water interface with 1 *wt.%* bulk solute concentration. Here, the  
 357 oil droplets undergo elongation at the interface (distance = 0  $\mu m$ ) but eventually  
 358 recover their shape as they are completely engulfed in the ice. In contrast, from  
 359 Fig.7D we notice that the larger  $R_2$  droplets do not undergo any type of deformation  
 360 at the same solute concentration of 1 *wt.%*. Hence, the elongation profile  
 361 of  $R_2$  droplets remains unmodified during the droplet-interface confrontation.

362 We deduce from these observations that the droplets confronting an ap-

363 proaching interface have distinct behaviours depending on the concentration of  
364 solute in the bulk solution. In particular, an increasing solute concentration  
365 tends to decrease the droplet elongation significantly.

366 Several experimental and theoretical studies devoted to the shape of bubbles  
367 during solidification in the absence of surfactant can be found in the literature  
368 [41–43]. Highly elongated bubbles along with the formation of a highly curved  
369 tip at the bubble-ice interface were observed [41, 42] and are controlled by the  
370 contact angle between the bubbles and the ice-water interface [43]. In the  
371 case of the low surfactant concentrations, we see from Fig.6A that the contact  
372 angle between the droplets and the ice-water interface remains close to  $90^\circ$   
373 during engulfment, similarly to bubbles, because of the weak thermal flux in  
374 the droplets owed to their low thermal conductivity in comparison to water  
375 [44]. This results in tear-shaped drops which are very similar to those reported  
376 in the literature for bubbles.

377 At higher surfactant concentration we observe much lower elongations. Ac-  
378 cording to Eq.1, an increasing bulk solute concentration ( $C_0$ ) implies a higher  
379 concentration of the solute segregated ( $C_0/K_0$ ) at the solid-liquid interface. The  
380 segregation of solute is further enhanced owing to an obstruction of their diffu-  
381 sion field by the droplets in the vicinity of the solid-liquid interface [12, 45]. The  
382 segregated solute, trapped in the layer between the droplet and the interface, in-  
383 duces solute premelting [46, 47] (Fig.2B at  $t = 44$  s, Fig.6B at  $t = 8$  s, in Fig.6C  
384 at  $t = 3$  s) which in turn causes a lowering of the equilibrium melting tempera-  
385 ture of water. Therefore these premelted films are stable below the solid’s bulk  
386 melting temperature,  $T_m$  and the thickness of the premelted films increases with  
387 the solute concentration [17, 46]. As a premelting film intercalates between the  
388 droplets and the solid liquid interface, the situation is very different from the  
389 literature studies discussed above as no finite contact angle between the drops  
390 and the interface can be defined. Here we suggest that the liquid-liquid interfa-  
391 cial tension between the droplet and the premelting film favors spherical shapes  
392 to minimize the interfacial area. Interestingly we note that the effect of size is

393 different at low and high surfactant concentrations. At low surfactant concen-  
394 trations, smaller droplets undergo a lower deformation, probably because of a  
395 higher capillary pressure inside the drops that opposes the deformation. At op-  
396 posite, for large surfactant concentrations, smaller droplets present a transient  
397 deformation, while larger droplets remain mostly spherical. This effect may be  
398 linked to the stronger segregation of solute in the films between the droplets  
399 and the ice in the case of larger films.

400 The deformation of droplets at the ice-water interface depends strongly on  
401 the growth rate ( $V_{st}$ ) and the corresponding bulk solute concentration ( $C_0$ ).  
402 Furthermore, the addition of solute increases the thickness of the observable  
403 premelted films, which appears to act as a protection mechanism against the  
404 interface initiated droplet deformation. The local solute environment and de-  
405 formation are two important criterion for cryopreservation in particular. In  
406 cryobiology, the excess of solute causes severe osmotic stresses that can insti-  
407 gate cell membrane rupture and hence, cryoinjury to cells and tissues [4, 19].  
408 In food engineering, alterations to the continuous phase concentration or to the  
409 shape and size of dispersed droplets is detrimental to the freeze-thaw stability  
410 of consumable emulsions [8]. Hence, a complete understanding of the solute  
411 redistribution mechanisms along with the associated object deformation at the  
412 corresponding freezing conditions is desired. Our multi-dimensional approach  
413 highlights the importance of different solidification parameters and the ubiq-  
414 uitous role of solute in dominating the various aspects of object deformation  
415 behaviour. Further work is required to accurately estimate the direction and  
416 magnitude of forces at the origin of the observed deformation.

### 417 **3.3 Droplets in Ice**

418 We have discussed so far the dynamics and consequences of oil droplets interact-  
419 ing with an approaching ice-water interface. In the last section, we investigate  
420 the fate of droplets after their engulfment by the ice front.

421 At 1 *wt.*% solute in the aqueous solution, at a growth rate of  $1 \mu\text{m} \cdot \text{s}^{-1}$ , the

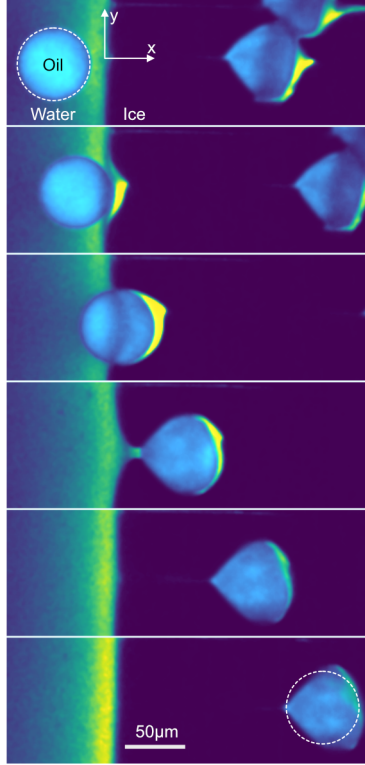


Figure 8: **Crushing of oil droplets during their engulfment in ice at a growth rate of  $V_{sl} = 1 \mu m \cdot s^{-1}$  with 1 wt% solute in solution.  $R_2 = 30.9 \pm 1.2 \mu m$ .** Typical time-lapse montage depicting the crushing of an oil droplet, scale bar =  $50 \mu m$ , time interval between frames: 60s. The dashed circle indicate the shape of the droplet before encapsulation. Note that in the crushing regime, the droplets are elongated in a direction parallel to the front, unlike in the other regimes (elongation perpendicular to the front). © (2020) S. Tyagi *et al.* (10.6084/m9.figshare.14815083) CC BY 4.0 license <https://creativecommons.org/licenses/by/4.0/>.

422 droplets undergo an elongation process after engulfment whereby the two radii,  
 423 along  $\vec{x}$  and  $\vec{y}$ , are stretched in magnitude as the droplets progress further in  
 424 ice. This means that the droplets flatten in the z direction as they are engulfed  
 425 in the ice. We depict this phenomenon with a time-lapse montage, highlighting  
 426 the deformation, in Fig.8. Interestingly, we observe this phenomenon only at a  
 427 growth rate of  $1 \mu m \cdot s^{-1}$  in the presence of 1 wt.% bulk solute concentration  
 428 for both droplets radii R1 and R2.

429 We currently have no definitive explanations for this behavior. One possibil-

430 ity could be that the shape of the water/ice meniscus in these conditions (curved  
431 meniscus) may favor entrapment and flattening of the droplets between the ice  
432 and the glass surface. However, this particular point would deserve additional  
433 experiments, in particular in 3D, which are beyond the scope of the current  
434 study.

435 Furthermore we note that once the droplets are trapped in the ice, we do  
436 not observe any thermal regelation, i.e the droplets do not manifest any motion  
437 relative to the ice. Moreover the liquid layer between the droplet from the  
438 growing solid decreases in thickness as the droplets move along the temperature  
439 gradient in ice towards an increasing undercooling ( $\Delta T = T_m - T$ , where  $T$  is  
440 the temperature of the substrate) [1]. The study of particle migration in ice is an  
441 important topic of research to understand frost heave, glacier motion, and ice-  
442 core dating among other technological applications [1]. Recent studies suggest  
443 that the presence of impurities or solutes tend to accelerate the *regelation* of  
444 trapped particles in ice. Typical migration velocities of  $0.1 \mu\text{m}\cdot\text{s}^{-1}$  at  $\Delta T$  of  $1 \text{ K}$   
445 have been reported for micron sized particles in the presence of impurities [48].  
446 Another recent study highlights the major impact of impurities on the rapid  
447 displacement ( $0.5 \text{ cm}$ ) over small time scales ( $120 \text{ s}$ ) of  $1 \mu\text{m}$  silicon particles  
448 trapped in ice [49]. The objects investigated here are 1 order of magnitude (or  
449 more) larger, which could explain why no regelation was observed. The use of  
450 cryo-confocal microscopy with the ability to image the solute segregation has  
451 a promising prospect for investigating such mechanisms. We believe the high  
452 space and temporal resolution can be used effectively to resolve the dynamics  
453 of individual colloidal particles to gain further insight into *regelation*.

## 454 4 Conclusions

455 In conclusion, we report that the oil droplets undergoing directional solidifica-  
456 tion feel the impact of solute at every stage, from being in the liquid phase to  
457 getting captured by the growing ice-water interface. The solute plays an impor-

458 tant role in determining the droplet shape (deformed or not), droplet behaviour  
459 (engulfment or rejection), and eventually the droplet spatial distribution. To  
460 predict the solidified microstructure, an understanding of the several in-situ  
461 mechanisms at play is therefore indispensable. The use of rapid cryo-confocal  
462 microscopy facilitates an *in situ* investigation and quantification of solidifica-  
463 tion mechanisms with visualization of the local solute segregation. To represent  
464 the observations in real-life systems, we need to explore models incorporating  
465 interaction dynamics and object behaviour with solute effects. Current theories  
466 do not encompass all the factors required for explaining the long-range solute  
467 effects on the objects during solidification. We hope our experimental data can  
468 serve to improve the existing theoretical models. Finally, we suggest that the  
469 freezing of oil-in-water emulsions may serve as an analogue for studying the *in*  
470 *situ* interaction of foreign objects with an advancing solid-liquid interface in the  
471 presence of solute effects.

## 472 **Acknowledgements**

473 The research leading to these results has received funding from the ANRT and  
474 Saint-Gobain through a CIFRE fellowship ( $N^{\circ}$  2017/0774). We would like to  
475 thank Alban Sauret and Virgile Thievenaz for discussing the deformation of  
476 droplets.

## 477 **Author contributions**

478 S.D. and C.M. designed and supervised the project, S.D, C.M. and S.T. designed  
479 the experiments, S.T. carried out the confocal microscopy, S.T., C.M. and S.D.  
480 analyzed the data. All authors discussed the results and implications and wrote  
481 the manuscript.

## 482 **Corresponding Authors**

483 Correspondence should be sent to Cécile Monteux (Cecile.Monteux@espci.fr)  
484 and Sylvain Deville (sylvain.deville@univ-lyon1.fr)

## 485 **Conflict of interest**

486 The authors declare no conflict of interest.

## 487 **Availability of materials and data**

488 The datasets generated during and/or analysed during the current study are  
489 available from the corresponding author on reasonable request.

## 490 **References**

- 491 [1] J. G. Dash, A. W. Rempel, and J. S. Wettlaufer. The physics of pre-  
492 melted ice and its geophysical consequences. *Reviews of Modern Physics*,  
493 78(3):695–741, 2006.
- 494 [2] M Shafiur Rahman. *Handbook of food preservation*. CRC press, 2007.
- 495 [3] VL Bronstein, YA Itkin, and GS Ishkov. Rejection and capture of cells  
496 by ice crystals on freezing aqueous solutions. *Journal of Crystal Growth*,  
497 52:345–349, 1981.
- 498 [4] C Körber. Phenomena at the advancing ice-liquid interface: solutes, parti-  
499 cles and biological cells. *Quarterly reviews of biophysics*, 21:229–298, 1988.
- 500 [5] Lifeng Zhang. Nucleation, growth, transport, and entrapment of inclusions  
501 during steel casting. *Jom*, 65(9):1138–1144, 2013.
- 502 [6] H Li, EA Ghezal, A Nehari, G Alombert-Goget, A Brenier, and K Lebbou.  
503 Bubbles defects distribution in sapphire bulk crystals grown by czochralski  
504 technique. *Optical Materials*, 35(5):1071–1076, 2013.

- 505 [7] Sylvain Deville. Freeze-casting of porous ceramics: a review of current  
506 achievements and issues. *Advanced Engineering Materials*, 10(3):155–169,  
507 2008.
- 508 [8] Supratim Ghosh and John N Coupland. Factors affecting the freeze-thaw  
509 stability of emulsions. *Food Hydrocolloids*, 22(1):105–111, 2008.
- 510 [9] OM Bunoiu, Th Duffar, and I Nicoara. Gas bubbles in shaped sapphire.  
511 *Progress in crystal growth and characterization of materials*, 56(3-4):123–  
512 145, 2010.
- 513 [10] D. Shangguan, S. Ahuja, and D. M. Stefanescu. An analytical model for  
514 the interaction between an insoluble particle and an advancing solid/liquid  
515 interface. *Metallurgical Transactions A*, 23(2):669–680, 1992.
- 516 [11] R. Asthana and S. N. Tewari. The engulfment of foreign particles by a  
517 freezing interface. *Journal of Materials Science*, 28(20):5414–5425, 1993.
- 518 [12] J. K. Kim and P. K. Rohatgi. The effect of the diffusion of solute between  
519 the particle and the interface on the particle pushing phenomena. *Acta*  
520 *Materialia*, 46(4):1115–1123, 1998.
- 521 [13] Adrian V. Catalina, Subhayu Sen, Doru M. Stefanescu, and William F.  
522 Kaukler. Interaction of porosity with a planar solid/liquid interface. *Met-*  
523 *allurgical and Materials Transactions A*, 35(5):1525–1538, 2004.
- 524 [14] Sidhanth Tyagi, Hélène Huynh, Cécile Monteux, and Sylvain Deville. Ob-  
525 jects interacting with solidification fronts: Thermal and solute effects. *Ma-*  
526 *terialia*, 12(April):100802, 2020.
- 527 [15] Justin C. T. Kao and Alexander A. Golovin. Particle capture in binary  
528 solidification. *Journal of Fluid Mechanics*, 625(September 2008):299, 2009.
- 529 [16] Yi Yang, JW Garvin, and HS Udaykumar. Sharp interface numerical simu-  
530 lation of directional solidification of binary alloy in the presence of a ceramic



- 531 particle. *International journal of heat and mass transfer*, 51(1-2):155–168,  
532 2008.
- 533 [17] JS Wettlaufer and M Grae Worster. Premelting dynamics. *Annu. Rev.*  
534 *Fluid Mech.*, 38:427–452, 2006.
- 535 [18] Dmytro Dedovets, Cécile Monteux, and Sylvain Deville. Five-dimensional  
536 imaging of freezing emulsions with solute effects. *Science*, 360(6386):303–  
537 306, 2018.
- 538 [19] Gregory M. Fahy. The relevance of cryoprotectant "toxicity" to cryobiology.  
539 *Cryobiology*, 23(1):1–13, 1986.
- 540 [20] J. A. Sekhar and R. Trivedi. Solidification microstructure evolution in the  
541 presence of inert particles. *Materials Science and Engineering A*, 147(1):9–  
542 21, 1991.
- 543 [21] Jürgen Pötschke and Volker Rogge. On the behaviour of foreign particles at  
544 an advancing solid-liquid interface. *Journal of Crystal Growth*, 94(3):726–  
545 738, 1989.
- 546 [22] A. W. Rempel and M. G. Worster. Interaction between a particle and an  
547 advancing solidification front. *Journal of Crystal Growth*, 205(3):427–440,  
548 1999.
- 549 [23] A. W. Rempel and M. G. Worster. Particle trapping at an advancing  
550 solidification front with interfacial-curvature effects. *Journal of Crystal*  
551 *Growth*, 223(3):420–432, 2001.
- 552 [24] Min S. Park, Alexander A. Golovin, and Stephen H. Davis. The encapsula-  
553 tion of particles and bubbles by an advancing solidification front. *Journal*  
554 *of Fluid Mechanics*, 560:415–436, 2006.
- 555 [25] P. S. Wei and S.Y. Y. Hsiao. Pore shape development from a bubble cap-  
556 tured by a solidification front. *Int. J. Heat Mass Transf.*, 55(25-26):8129–  
557 8138, dec 2012.

- 558 [26] E. A. Ghezal, H. Li, A. Nehari, G. Alombert-Goget, A. Brenier, K. Leb-  
559 bou, M. F. Joubert, and M. T. Soltani. Effect of pulling rate on bubbles  
560 distribution in sapphire crystals grown by the micropulling down ( $\mu$ -PD)  
561 technique. *Crystal Growth and Design*, 12(8):4098–4103, 2012.
- 562 [27] H. Jamgotchian, R. Trivedi, and B. Billia. Interface dynamics and cou-  
563 pled growth in directional solidification in presence of bubbles. *Journal of*  
564 *Crystal Growth*, 134(3-4):181–195, 1993.
- 565 [28] S. Sen, W. F. Kaukler, P. Curreli, and D. M. Stefanescu. Dynamics of  
566 solid/liquid interface shape evolution near an insoluble particle - An X-ray  
567 transmission microscopy investigation. *Metallurgical and Materials Trans-*  
568 *actions A: Physical Metallurgy and Materials Science*, 28(10):2129–2135,  
569 1997.
- 570 [29] F López Arbeloa, P Ruiz Ojeda, and I López Arbeloa. Fluorescence self-  
571 quenching of the molecular forms of rhodamine b in aqueous and ethanolic  
572 solutions. *Journal of luminescence*, 44(1-2):105–112, 1989.
- 573 [30] Rex Malcolm Chaplin Dawson, Daphne C Elliott, William H Elliott, and  
574 Kenneth M Jones. *Data for biochemical research*, volume 3. Clarendon  
575 Press, 2002.
- 576 [31] Eleanor LV Harris, S Angal, and Simon Roe. *Protein purification applica-*  
577 *tions: a practical approach*, volume 71. IRL press Oxford, 1990.
- 578 [32] Alan D McNaught, Andrew Wilkinson, et al. *Compendium of chemical*  
579 *terminology*, volume 1669. Blackwell Science Oxford, 1997.
- 580 [33] Johannes Schindelin, Ignacio Arganda-Carreras, Erwin Frise, Verena  
581 Kaynig, Mark Longair, Tobias Pietzsch, Stephan Preibisch, Curtis Rueden,  
582 Stephan Saalfeld, Benjamin Schmid, et al. Fiji: an open-source platform  
583 for biological-image analysis. *Nature methods*, 9(7):676, 2012.

- 584 [34] Stéfan van der Walt, Johannes L. Schönberger, Juan Nunez-Iglesias,  
585 François Boulogne, Joshua D. Warner, Neil Yager, Emmanuelle Gouillart,  
586 Tony Yu, and the scikit-image contributors. scikit-image: image processing  
587 in Python. *PeerJ*, 2:e453, 6 2014.
- 588 [35] Dmytro Dedovets, Cécile Monteux, and Sylvain Deville. A temperature-  
589 controlled stage for laser scanning confocal microscopy and case studies in  
590 materials science. *Ultramicroscopy*, 195(August):1–11, 2018.
- 591 [36] W. A. Tiller, K. A. Jackson, J. W. Rutter, and B. Chalmers. The redistribu-  
592 tion of solute atoms during the solidification of metals. *Acta Metallurgica*,  
593 1(4):428–437, 1953.
- 594 [37] JL Anderson, ME Lowell, and DC Prieve. Motion of a particle generated by  
595 chemical gradients. part 1. non-electrolytes. *J. Fluid Mech*, 117(1):107–121,  
596 1982.
- 597 [38] Rodrigo Nery-Azevedo, Anirudha Banerjee, and Todd M Squires. Diffusio-  
598 phoresis in ionic surfactant gradients. *Langmuir*, 33(38):9694–9702, 2017.
- 599 [39] Trevor J Shimokusu, Vanessa G Maybruck, Jesse T Ault, and Sang-  
600 woo Shin. Colloid separation by co2-induced diffusiophoresis. *Langmuir*,  
601 36(25):7032–7038, 2019.
- 602 [40] Suin Shim and Howard A Stone. Co2-leakage-driven diffusiophoresis causes  
603 spontaneous accumulation of charged materials in channel flow. *Proceedings*  
604 *of the National Academy of Sciences*, 117(42):25985–25990, 2020.
- 605 [41] P. S. Wei, C.C. Huang, Z.P. Wang, K.Y. Chen, and C.H. Lin. Growths  
606 of bubble/pore sizes in solid during solidification—an in situ measurement  
607 and analysis. *J. Cryst. Growth*, 270(3-4):662–673, 2004.
- 608 [42] Norizaku Maeno. Air bubble formation in ice crystals. *Phys. Snow Ice*  
609 *Proc.*, 1(1):207–2181, 1967.

- 610 [43] P. S. Wei and C.Y Ho. An Analytical Self-Consistent Determination of a  
611 Bubble with a Deformed Cap Trapped in Solid during Solidification. *Metall.*  
612 *Mater. Trans. B*, 33(February):91–100, 2002.
- 613 [44] AA Chernov, DE Temkin, and AM Mel’Nikova. The influence of the ther-  
614 mal conductivity of a macroparticle on its capture by a crystal growing  
615 from a melt. *Sov. Phys. Crystallogr*, 22(6):656–658, 1977.
- 616 [45] R. Sasikumar and T. R. Ramamohan. Distortion of the temperature and  
617 solute concentration fields due to the presence of particles at the solidifi-  
618 cation front-effects on particle pushing. *Acta Metallurgica Et Materialia*,  
619 39(4):517–522, 1991.
- 620 [46] J. Wettlaufer. Impurity Effects in the Premelting of Ice. *Physical Review*  
621 *Letters*, 82(12):2516–2519, 1999.
- 622 [47] A. W. Rempel, J. S. Wettlaufer, and M. G. Worster. Interfacial Premelt-  
623 ing and the Thermomolecular Force: Thermodynamic Buoyancy. *Physical*  
624 *Review Letters*, 87(8):088501, 2001.
- 625 [48] Julia Schollick. *Real space study of pattern formation in freezing colloidal*  
626 *suspensions*. PhD thesis, University of Oxford, 2012.
- 627 [49] Navaneeth K. Marath and J. S. Wettlaufer. Impurity effects in thermal  
628 regelation. *Soft Matter*, 16(25):5886–5891, 2020.

## 5 Supplementary Information

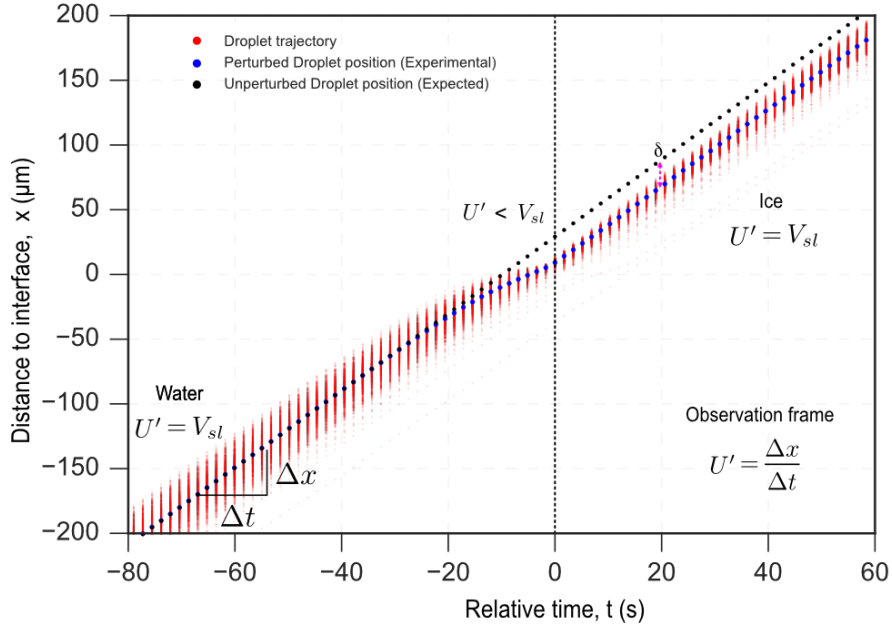


Figure S1: **Measurement of interaction time and apparent droplet velocity  $U'$  in the observation frame.** In the observation frame, far from the solid-liquid interface in water the droplet moves at the imposed growth rate  $U' = Dx/Dt = V_{sl}$ , as the droplet approaches the interface it gets repelled  $U' \neq V_{sl}$ , and as the droplet is engulfed in the ice it doesn't get repelled anymore, thereby recovering  $U' = V_{sl}$ . The interaction time is the total duration over which a droplet gets repelled by the solidification interface. Relative time is zero when the front edge of the droplet hits the solidification front. Experimental conditions for which the curve was recorded:  $V_{sl} = 3 \mu\text{m} \cdot \text{s}^{-1}$ ,  $G = \nabla T = 10^4 \text{ K} \cdot \text{m}^{-1}$ , Droplet size  $R_1 = 7.2 \pm 0.4 \mu\text{m}$ . © (2020) S. Tyagi *et al.* (10.6084/m9.figshare.14815083) CC BY 4.0 license <https://creativecommons.org/licenses/by/4.0/>.

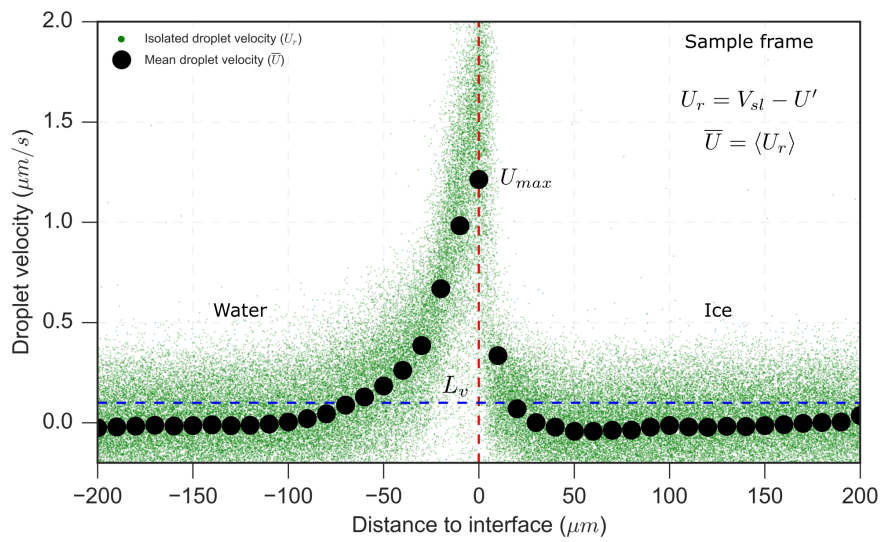


Figure S2: **Deducing the isolated droplet velocity  $U_r$  and the mean droplet velocity  $\bar{U}$  in the sample frame.** In the sample frame, the isolated droplet velocity  $U_r$  is zero far from the interface, it increases and reaches a maximum when the droplet gets repelled by the interface and subsequently, reduces to zero as the droplet is engulfed in the ice. Experimental conditions for which the curve was recorded:  $V_{sl} = 3 \mu m \cdot s^{-1}$ ,  $G = \nabla T = 10^4 K \cdot m^{-1}$ , Droplet size  $R_1 = 7.2 \pm 0.4 \mu m$ . © (2020) S. Tyagi *et al.* (10.6084/m9.figshare.14815083) CC BY 4.0 license <https://creativecommons.org/licenses/by/4.0/>.